Convective Delivery of Electroactive Species to Annular Nanoband Electrodes Embedded in Nanocapillary-Array Membranes

*Larry R. Gibson II, Sean P. Branagan, and Paul W. Bohn**

Significant technological drivers motivate interest in the use of reaction sites embedded within nanometer-scale channels, and an important class of these structures is realized by an embedded annular nanoband electrode (EANE) in a cylindrical nanochannel. In this structure, the convective delivery of electroactive species to the nanoelectrode is tightly coupled to the electrochemical overpotential via electroosmotic flow. Simulation results indicate that EANE arrays significantly outperform comparable microband electrode/microchannel structures, producing higher conversion efficiencies at low Peclet number. The results of this in-depth analysis are useful in assessing possible implementation of the EANE geometry for a wide range of electrochemical targets within microscale total analysis systems.

1. Introduction

Over the past two decades, nanoelectrodes have been heavily exploited to understand molecular interactions in confined geometries as they exist in nature,[1] and in applications including biomolecular sensing,[2–4] establishment of ion enrichment and depletion regions for enhanced chemical processing,[5] controlled electrokinetic fluid transport,[6,7] and fundamental electrochemical studies.[8,9] Significant practical advantages, including enhanced electron-transfer current, have been observed as the dimension of the nanoelectrode approaches the diffusive scaling length.[10–12] This benefit, as measured by the faradaic current produced, is critically dependent on the nanoelectrode geometry.[13–15] In addition, redox cycling, parallelization, and nanofluidic confinement may all be used to enhance sensitivity in analytical electrochemistry.[16–21]

Indeed, in all of the above nanoscale implementations of electrochemistry, significant enhancements are realized for electrochemical analysis. Ultimately, however, all are limited by diffusive transport of the electroactive species to the electrode surface. Convective delivery of reagents is well known to reduce this limitation by collapsing the diffusive boundary layer.[22] Rotating ring-disk electrodes are a classical example and, more recently, a wide variety of electrodes embedded within capillary electrophoresis detection systems have been used with great success.[23] In fact, controlled hydrodynamic voltammetry achieved with pressure-driven flow in microchannels has been thoroughly characterized using finite element simulations.[24–26] Convective delivery of electroactive species to the electrode is nominally applicable to nanoband/nanoelectrode systems, as well. For example, recent work from our laboratory showed that the coupling of convective fluidic transport and electrochemistry in planar nanochannels is useful for *in situ* generation of reagents for on-chip reactions, such as hydrogenation reactions.[27] Fritsch and co-workers have demonstrated similar electrochemical enhancement by convection using magnetohydrodynamics.[28] However, a

L. R. Gibson II, Dr. S. P. Branagan
Department of Chemical and Biomolecular Engineering
University of Notre Dame
Notre Dame, IN 46556, USA
Prof. P. W. Bohn
Department of Chemical and Biomolecular Engineering
Department of Chemistry and Biochemistry
318 Stinson-Remick Hall
University of Notre Dame
Notre Dame, IN 46556, USA
Email: pbohn@nd.edu

DOI: 10.1002/smll.201200237

small NANO MICRO

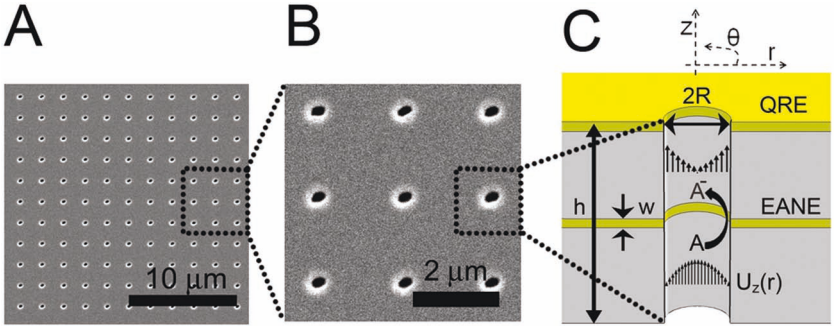

Figure 1. Embedded annular nanoband electrodes (EANEs) within nanocapillary-array membranes (NCAMs): geometric characterization and cross-sectional schematic. A)Scanning electron microscopy image showing the quasi-reference electrode (QRE) surface in a typical 11 × 11 array of nanocapillaries; B) enhanced magnification. C)Cross-sectional schematic of a single EANE sandwiched by two polymer layers, capped by a second Au layer acting as the QRE. The radius *R*, electrode width *w*, and nanocapillary height *h* are defined as shown. Typical values of these geometric parameters simulated are 0.01 µm < *w* < 1.0 µm, 0.1 µm < *R* < 1 µm, and *h* ≈15 µm.

single nanoband/nanochannel (or even several acting in parallel) can never match the processing power and throughput of a microchannel, owing to the reduced cross-sectional area of a nanochannel compared to a microchannel. In contrast, simultaneous processing of hundreds, or even thousands, of nanochannels in parallel can increase the throughput to practical levels.[29] In nanochannels, molecular transport is accomplished via electroosmotic flow (EOF), which offers the benefits of no moving parts and a relatively low pressure-drop. In addition, a relatively small applied potential is required to achieve linear fluid flow rates comparable to pressure-driven microfluidic channels. Also, in contrast to conventional hydrodynamic voltammetry in microfluidic architectures, the same pair of electrodes can be used for both EOF and electrochemistry without causing adverse side reactions, most importantly, electrolysis of water and accompanying bubble nucleation. For example, a typical overpotential of 1 V is sufficient to drive both electrokinetic transport and electrochemical reactions in aqueous solution without bubble nucleation. The element that enables these advances is the embedded annular nanoband electrode (EANE, see **Figure 1**), which is fabricated into a multilayer membrane presenting an array of 121 nanofluidic channels, each of which supports an EANE.[29] Prior results have shown that the rate of conversion of $Fe(CN)_6^{4-}$ to $Fe(CN)_6^{3-}$ at the EANE is far superior with electrokinetically enhanced convective transport than with diffusive transport alone.[29]

Herein, the applicability of the EANE is studied by dimensional analysis with the aim of understanding the behavior of EANE arrays over a wide range of electrochemical operating conditions. Conventional fluid dynamics are applied in a cylindrical coordinate system, and key nondimensional parameters are identified. Using a combination of experimental results and finite element simulations, the effect of the electrode surface area on the electron-transfer reaction in the presence of convection is described, and the conditions under which the nanoreactor can accommodate high-throughput reactions are identified. The use of a single pair of electrodes for both EOF and electrochemistry is further explored by comparing the EANE to a similar configuration in a microchannel, and the two structures are evaluated under comparable operating conditions. Operating at the highest accessible overpotential before unwanted electrochemical reactions occur, the geometric and electrokinetic transport conditions required for optimal faradaic current produced by convective delivery of electrochemical reagents are identified.

2. Theory

A one-electron electron-transfer reaction, such as $Fe(CN)_6^{3-/4-}$, can be simplified to a generic reaction for these purposes (A to A^-), as shown by $A + e^- \rightleftharpoons A^-$

For the cylindrical coordinate system depicted in Figure 1, the time-dependent flux of species A may be reduced to the form given in Equation (1):

$$\frac{\partial C_A}{\partial t} + v_z(r)\frac{\partial C_A}{\partial_z} = D_A\left[\frac{1}{r}\frac{\partial}{\partial_r}\left(r\frac{\partial C_A}{\partial r}\right)\right] \quad (1)$$

where C_A and D_A are the concentration and diffusion coefficient of the reactant A, respectively, and $v_z(r)$ is the axial velocity as a function of radial position. Note that the reaction term, r_A, typically included in the equation of continuity is omitted from Equation (1), but is later added as a boundary condition at the reaction site. The equation of motion may be simplified by assuming Stokes' flow to give:

$$\frac{\partial p}{\partial z} - F = \mu\left[\frac{1}{r}\frac{\partial}{\partial r}\left(r\frac{\partial v_z}{\partial r}\right)\right] \quad (2)$$

where p describes the pressure drop across the nanochannel and the vector F, which describes the electrokinetic force term, is accounted for by imposing a slip-velocity (v) boundary condition on the nanopore wall approximated by Smulochowski[30,31] as

$$v \mid_{r=R} = \mu_{eo} E \quad (3)$$

Here, μ_{eo} represents the polymer-specific electroosmotic mobility term and E describes the electric field established between the working and quasi-reference electrodes.

In Figure 1, the electroosmotic velocity profile is established by the potential between the QRE and the EANE, which is the same potential driving the electrochemical reaction. Electroosmosis is strictly established only between the EANE and the QRE, but a viscous drag causes a significant back-pressure within the section of the nanochannel located below the EANE. Continuity is satisfied by the pressure-driven flow profile within the bottom portion of the nanopore. Analytical solutions for the combined EOF and pressure-driven flows, vz(r), are poorly adapted to this

specific regime.[32] Therefore the flow velocity field, defined here as $U_z(r)$, is obtained computationally.

Substituting $U_z(r)$ into Equation (3) gives the governing equation for the EANE reactor:

$$\frac{\partial C_A}{\partial t} = D_A\left[\frac{1}{r}\frac{\partial}{\partial r}\left(r\frac{\partial C_A}{\partial r}\right)\right] - U_z(r)\frac{\partial C_A}{\partial z} \quad (4)$$

To extend the utility of these calculations beyond the specific dimensions of the nanoscale devices used in this study, nondimensional parameters are introduced:

$$r^* = \frac{r}{R};\ C_A^* = \frac{C_A}{C_{A_0}};\ z^* = \frac{z}{R};\ \tau^* = \frac{D_A t}{R^2};\ U_z^* = \frac{RU_z}{D_A}$$

where R represents the nanochannel radius, and h and w give the nanopore height and electrode width, as shown in Figure 1. Substituting the nondimensional quantities into Equation (4) affords the dimensionless form of the governing equation:

$$\frac{\partial C_A^*}{\partial \tau^*} = \left[\frac{1}{r^*}\frac{\partial}{\partial r^*}\left(r^*\frac{\partial C_A^*}{\partial r^*}\right)\right] - U_z^*(r^*)\frac{\partial C_A^*}{\partial z^*} \quad (5)$$

Due to the high concentration (1.0 M) of running buffer in the experimental work, the Debye length κ^{-1} is sufficiently small that $\kappa R >> 1$.[33] In this regime ion transport is dominated by electroosmosis mediated by the potential applied between the QRE and the EANE.

For each mesh element in the model geometry depicted in Figure 1, the simulations report J_A, U_z, C_A, and E, where J_A is the flux of reactant species A. Experimentally comparable quantities are computed using Equation (6):

$$i = 2\pi RF\int_{-w/2}^{w/2} J_A|_{r=R}\,dz \quad (6)$$

and Equation (7)

$$U_{z,av} = \frac{\int_0^{2\pi}\int_0^R U_z(r)r\,dr\,d\theta}{\int_0^{2\pi}\int_0^R r\,dr\,d\theta} \quad (7)$$

where F is Faraday's constant. Due to the high buffer concentration in the reactor, electric double layer effects are negligible, and the charging current is nearly completely suppressed. As a result, i in Equation (6) represents the faradaic current, and $U_{z,av}$ from Equation (7) gives the average velocity in the nanopore.

From these computed values the following dimensionless quantities can be obtained directly:

$$W = \frac{w}{R} \quad (8)$$

W is a parameter describing the electrode size relative to the pore dimensions.

$$Pe = \frac{U_{z,av}R}{D_A} \quad (9)$$

Pe (Peclet number) describes the ratio of convective to diffusive transport of molecular species in fluidic environments. In the present case where combined EOF and electrochemical conversion occurs, Pe is tightly coupled to the overpotential by Equation (3). The nondimensional overpotential η^* may be defined by Butler–Volmer kinetics and represents the driving force for electrochemical conversion applied to the EANE:

$$\eta^* = \frac{\exp\left(\frac{nF}{RT}\eta\right)}{1+\exp\left(\frac{nF}{RT}\eta\right)} \quad (10)$$

where $\eta = E - E^0$, and E^0 is the equilibrium potential.

$$\varepsilon = 1 - \frac{C_A}{C_{A_0}}\left(r = 0;\ z = \frac{h}{4}\right) \quad (11)$$

ε (conversion efficiency) represents the ratio of the final product concentration to the theoretical maximum product concentration if full conversion were achieved. Equation (11) is defined by a concentration C_A measured downstream from the electrode, outside the diffusive boundary layer, where an accurate final product concentration is obtained. Intuitively, a trade-off is expected between ε and Pe; indeed, prior results by Amatore et al.[24] show that for pressure-driven flow above a microband electrode in a microchannel, greater Pe number results in more of the reagent being swept downstream past the electrode, thereby resulting in lower conversion efficiency. However, the relationship of Pe to ε is more complicated in the NCAM–EANE geometry investigated here, because the convective transport rate and the electrochemical driving force both vary with overpotential.

A final performance metric, ψ, describes the nondimensional faradaic current of the A/A^- reaction:

$$\psi = \frac{i}{2\pi RF D_A C_{A_0}} \quad (12)$$

ψ is scaled to the initial concentration, the diffusion coefficient, and the electrode length scale and, thus, describes the utilization of the electrode relative to the maximum achievable faradaic current under diffusion-limited conditions.

A critical question arises concerning the potential advantages of performing electrochemistry in nanoscale embedded reactors compared to the same reactions carried out in larger, planar microchannels. Thus, a separate model was developed simulating a microband electrode/microchannel geometry, which was used to calculate the performance metrics described above for comparison to the NCAM–EANE (see Supporting Information for a full theoretical discussion of the microchannel geometry). Unlike previous work in which micrometer-scale hydrodynamic voltammetry was performed using pressure-driven flow, the microband electrode/microchannel system described herein relies on induced EOF for convective transport. For this reason, the average velocity in the microchannel is considerably slower than that found in either the EANE or a typical pressure-driven microchannel, due to the smaller electric field between the working electrode and the QRE. However, operation under

small NANO MICRO

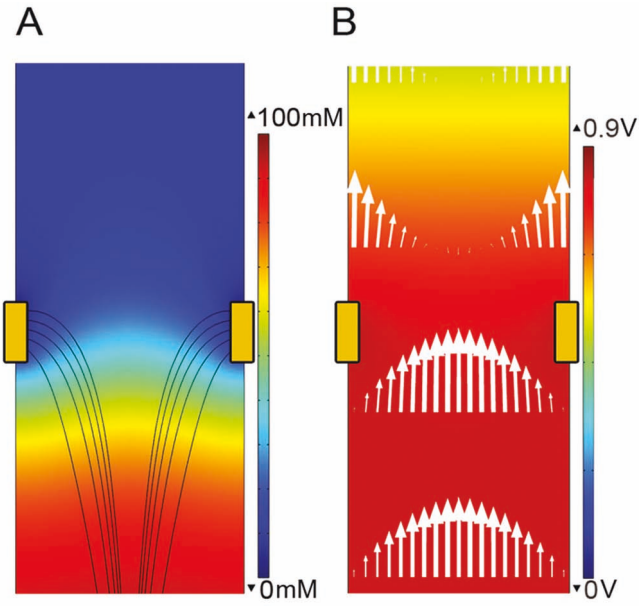

Figure 2. Results of simulated electrochemical conversion and induced electrokinetic flow, as shown by 2D cross sections in the immediate vicinity of the EANE. The position of the EANE is depicted by the gold rectangles near the mid-point in both panels. A) Surface plot (color): concentration profile of $Fe(CN)_6^{4-}$. Streamlines: flux of $Fe(CN)_6^{4-}$ towards the EANE. B) Surface plot (color): electrical potential gradient produced by the EANE–QRE electrode pair. Arrows: velocity profile.

these conditions is required to establish a valid basis for comparison of the NCAM–EANE and the microband electrode/microchannel system.

3. Results and Discussion

3.1. Simulation Results and Validation

Figure 2 shows the results of a typical simulation of combined electrochemical conversion and induced electrokinetic flow. Figure 2A shows how rapid radial diffusion from the center of the nanopore to the electrode surface nearly depletes the reagent species under conditions of high overpotential. Figure 2B shows the flow profile and distribution of electrical potential. The unique flow profile on the top side of the EANE is a result of the EOF boundary condition described in Equation (3), while the Poiseulle-type flow in the bottom of the nanochannel develops as a result of continuity.

Figure 3 shows experimental and simulated cyclic voltammograms (CVs) for a typical NCAM–EANE structure operating in a two-electrode configuration. The test solution contained 1.0 M KNO_3, 10 mM phosphate buffer at pH 7.2, and various concentrations of the reagent $[Fe(CN)_6^{3-}] = [Fe(CN)_6^{4-}] = 10, 25, 50$, and 100 mM, in Figure 3A–D, respectively. The NCAM–EANE configuration consisted of a

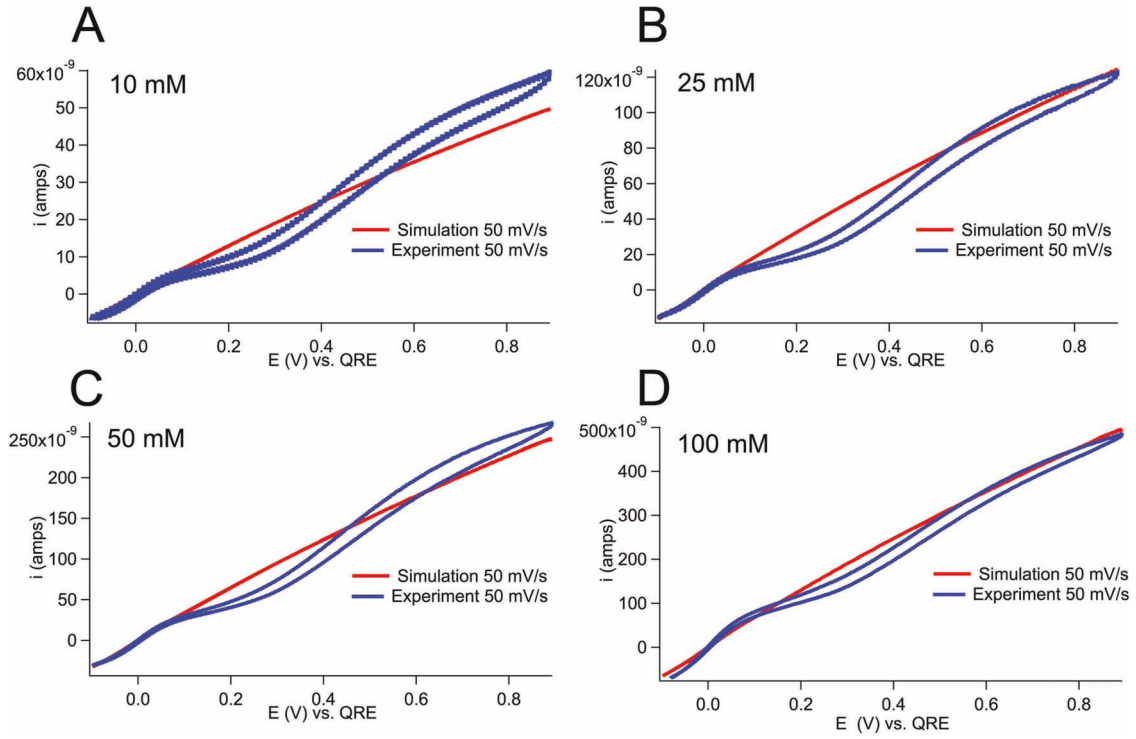

Figure 3. Validation of simulated curves against various experimental concentrations. Equilibrated experimental curves are shown in blue and simulated curves in red. All experiments were performed using an NCAM–EANE displaying 11 × 11 pores, $R \approx 600$ nm, $h \approx 15$ µm, and $w \approx 200$ nm. All solutions contained 1.0 M KNO_3, 10 mM phosphate buffer at pH 7.2, and various concentrations of $Fe(CN)_6^{4-}/Fe(CN)_6^{3-}$ as follows: A) 10, B) 25, C) 50, and D) 100 mM. Simulations were performed matching the experimental conditions.

single 11 × 11 array of pores (pore diameter 600 nm with 2.0 μm pitch) containing an EANE with thickness w = 200 nm. After equilibration, CVs were collected at 50 mV s^{-1} across the scan range –0.1 V < E < 0.9 V. Qualitatively, the CVs show an effective equilibrium potential $E_0 \approx 0.0$ V, visible in the CVs in Figure 3, and a linearly increasing current with increasing anodic overpotential, due to increasing EOF with overpotential. Very good agreement between the simulated and experimental curves is achieved across all concentrations, although some minor differences are observed relating to charging current and diffusive overlap between adjacent nanopores.

3.2. Range of Nondimensional Parameters Pe, *W*, and η^*

By design, the NCAM–EANE structure incorporates tight coupling of convective flow rate with electrochemical potential. The electric field strength which drives EOF can reach moderately high values, 1200 V cm^{-1}, due to the close spacing of the EANE and QRE, even at moderate applied potential (e.g., 0.9 V). The resulting EOF produces an average velocity that scales linearly with potential $U_{z,av} \approx E = \eta + E_0$. The average flow velocities are in the range $0 < U_{z,av} < 1.4$ mm s^{-1} across the scan range $0 < E < 0.9$ V. Linear flow rates of 1–2 mm s^{-1} are typical for pressure-driven microchannel flow, but the confined geometry of the NCAM limits the Peclet number to low values. Equation (9) defines the range as $0 < \mathrm{Pe} < 0.5$, which indicates that diffusive transport processes are important under all conditions used in this work. The electrochemical overpotential also changes linearly with E and Pe, where in this case $E = \eta$ since $E_0 \approx 0$. In principle, the intersection of zero overpotential may occur at any given Pe or $U_{z,av}$ depending on the equilibrium potentials of the half reactions occurring at each electrode. However, the nondimensional overpotential is the critical quantity for determining electrode performance; it scales nonlinearly $0 < \eta^* < 1$ in the potential window $0 < E < 0.3$ V, and then remains at $\eta^* \approx 1$ across the wide range of $0.3 \text{ V} < E < 0.9$ V. This high overpotential regime defines the conditions under which electron transfer is entirely transport limited.

Regardless of the electrochemical system, the annular geometry of the EANE defines the active area of the reaction site by the thickness w of the EANE layer deposited. Although a large reaction site is desirable from the perspective of conversion efficiency, fabrication of thick EANEs ($w \geq 1$ μm) using the current multilamellar film approach is impractical. Thus, the range of W investigated here is $0.04 < W < 4$, for both the EANE and microchannel systems.

3.3. Steady-State Current Dependence on Overpotential

An overpotential exists when the applied potential at the EANE exceeds that of the reduction potential for the $Fe(CN)_6^{4-}/Fe(CN)_6^{3-}$ redox couple (≈0 V vs. the QRE in these studies). The Butler–Volmer equation predicts that faradaic current increases exponentially with applied voltage at high overpotential. However, this does not take into account the influence of mass transport, whether it is convective or diffusive in origin. **Figure 4** compares the dimensionless current, ψ, for a nanochannel EANE array over a range of W and η^* values with EOF enabled and disabled. In practice the most straightforward approach to eliminating EOF is adjusting the pH to render the surface charge density ≈0. In Figure 4A and B, maximal current is observed at high overpotentials, $\eta^* \approx 1$, and dimensionless electrode widths above 1. However, in the optimal region of Figure 4A, ψ is approximately 18-fold larger than in the absence of EOF. It is worth noting that although ψ is clearly very sensitive to overpotential in the presence of EOF, it is exclusively mass transport limited along the line where $\eta^* \approx 1$. Thus, at high overpotential the electron-transfer rate (a function of the reaction-specific equilibrium potential, E^0) has little effect on ψ, making this region broadly applicable to a number of mass-transport-limited electrochemical reactions. In this rendering, the current increases linearly as the overpotential approaches unity, due to nondimensional treatment of the overpotential. Based on the experimental parameters, $\eta^* \approx 1$ is achieved over a wide range of applied potential of $0.3 \text{ V} < \eta < 0.9$ V, sufficient to achieve the mass-transfer limit of the $Fe(CN)_6^{4-}/Fe(CN)_6^{3-}$ redox couple.

3.4. Steady-State Conversion Efficiency

Qualitatively, the motivation for developing an array of embedded nanoelectrodes stems from the short diffusion

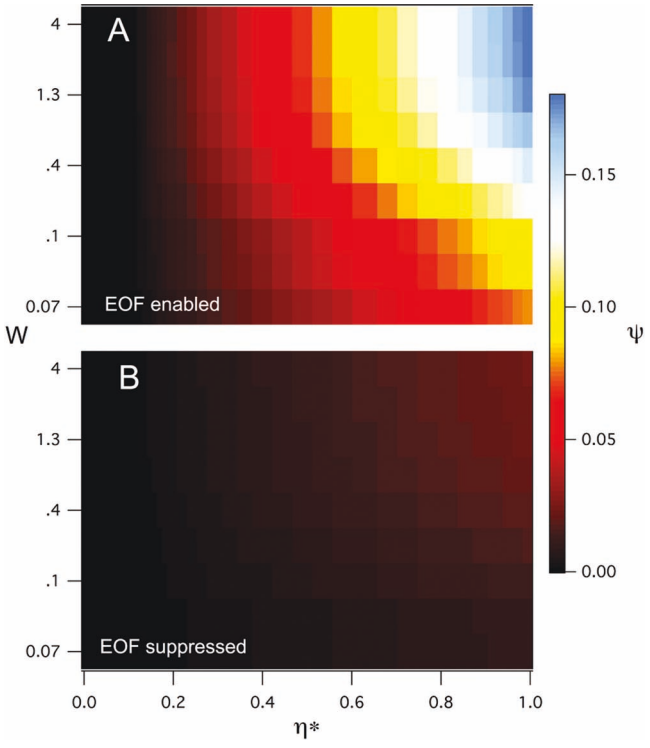

Figure 4. Dimensionless current ψ as a function of dimensionless electrode width W and dimensionless overpotential η^*, for the EANE–nanocapillary structure. A)EOF enabled. B)EOF suppressed. In the presence of favorable EOF and high overpotential, the current produced is significantly enhanced.

small NANO MICRO

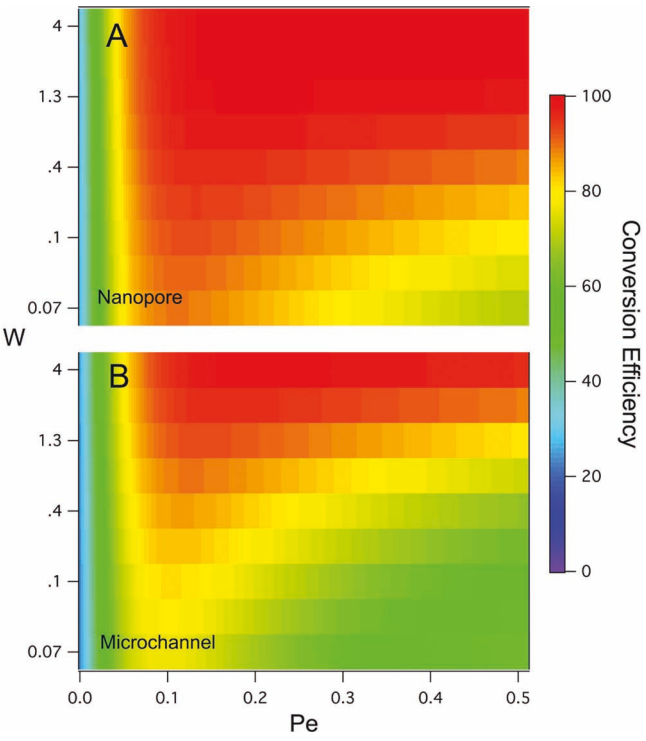

Figure 5. Surface plot depicting conversion efficiency as a function of the Peclet number and nondimensional electrode width. Since Pe and η^* are tightly coupled, the results are valid only for the present case where $E_0 \approx 0$ V, which occurs for the ferri-ferrocyanide reaction when the reverse reaction is responsible for electron transfer at the QRE. A) EANE–nanopore; B) microband electrode/microchannel.

distances required for molecules at any radial position to access the wall electrodes. Thus, the conversion efficiency is a key figure of merit regarding the quantity of product generated for downstream applications. **Figure 5** compares the maximum conversion efficiencies achieved in the NCAM–EANE geometry with that in a comparable microband electrode/microchannel geometry. At low Pe, due to low nondimensional overpotential, there is no discernible difference between the two geometries independent of size of the electrode, and minimal conversion is achieved. However, both geometries show a transition to W-dependent behavior near Pe ≈ 0.05, above which significant differences in conversion efficiency are observed. At higher Pe values it is possible to achieve 100% conversion efficiency at a range of electrode sizes in both the nanochannel and microchannel. However, much smaller relative electrode surface areas are required to achieve complete conversion in the nanochannel. Figure 5 reveals that maximum conversion efficiency of 100% is reached at W values of 2.5 and 0.5 for the microreactor and nanoreactor, respectively, and exceeding these values at high Pe provides no additional advantage. These findings indicate that essentially perfect conversion of reactants can be achieved in either geometry. However, NCAMs featuring EANEs achieve 100% conversion efficiency over a larger range of dimensionless parameters (Pe > 0.05, W > 0.5) than microchannel reactors (Pe > 0.05, W > 3), and, accounting for the normalization factor, it is clear that 100% conversion efficiencies can be achieved in the nanochannel geometry with considerably smaller electrodes.

3.5. Comparison of Performance Metrics

Table 1 provides a comparison of both dimensional and nondimensional parameters and steady-state performance metrics for the NCAM–EANE versus microband–microchannel. By design, the same nondimensional parameters, Pe ≈ 0.5 and W = 0.04, 0.4, and 4, were used for the NCAM–EANE and the microband–microchannel, thus providing a valid basis of comparison. In agreement with Figure 5, higher conversion efficiencies are observed for the NCAM–EANE than for the microchannel, under the same nondimensional conditions. This can be ascribed to the radial diffusion of species in the nanocapillary, compared to diffusion to a wall in the microband–microchannel geometry. However, the comparison becomes quite stark when considering dimensional quantities. Due to the close spacing of the electrodes, the linear flow rate in the EANE is approximately 100 times faster than that in the microchannel: 1.4 versus 0.014 mm s^{-1} in the microchannel.

Table 1. Comparison of NCAM – EANE and microband electrode/microchannel performance.

	Nondimensional				Dimensional				
	W	Pe[a]	ε	Ψ[b]	w	$U_{z,av}$[a] [mm s^{-1}]	i [nA]	Q[c] [pL s^{-1}]	F_A[c] [pmol s^{-1}]
NCAM–EANE, R = 250 nm, h = 15 µm, pitch = 2.0 µm	0.04	0.52	0.69	0.16	10 nm	1.4	1.5	165	11.4
	0.4		0.89	0.31	100 nm		3.06		14.7
	4		1.00	0.41	1 µm		4.03		16.5
microchannel/microband, $l = d$ = 50 µm, h = 3 mm	0.04	0.52	0.47	0.22	1 µm	0.0135	69	33	1.55
	0.4		0.66	0.42	10 µm		131		2.18
	4		0.95	0.82	100 µm		256		3.14

[a]The velocity (and thus Pe) is determined by the applied potential E = 0.9 V; [b]See Supporting Information for a theoretical description of $\psi_{microchannel}$; [c]For the NCAM–EANE, Q and F_A are calculated for a 50 µm × 50 µm membrane area containing approximately 600 pores, thus operating in the same cross-sectional area as the microchannel. F_A is calculated for a 100 mM starting concentration.

Unfortunately, achieving faster EOF in the microchannel would require a much larger driving potential than in the EANE, which would result in undesirable electrochemical side effects such as electrolysis. Alternatively, pressure-driven flow could be used to supplement the flow rate in a microchannel.[24] Operation at such a high Peclet number is a disadvantage for mass-transfer-limited electrochemical reactions, such as the $Fe(CN)_6^{4-}/Fe(CN)_6^{3-}$ model, which rely on the radial diffusion of electroactive species toward the reaction site. As a result, the conversion efficiency observed downstream of an EANE is higher than that observed for the same reaction implemented in either an EOF-driven microchannel (this work) or a similar microchannel undergoing pressure-driven hydrodynamic voltammetry.[29]

This still leaves the question of throughput, that is, the volumetric flow rate of solution capable of being processed by an NCAM–EANE compared to a microband electrode/microchannel system. Obviously, a single nanopore will never be able to process the same amount of fluid as the much larger microchannel, but it is a simple matter to operate hundreds or thousands of nanocapillaries in parallel. For an NCAM–EANE measuring 50 μm × 50 μm in size (the same cross-sectional area occupied by the microchannel), approximately $N = 600$ nanocapillaries could be arranged in parallel. Multiplying the number of pores by the cross-sectional area and the average velocity yields the total flow volumetric flow rate, $Q = N \cdot U_{z,av} \cdot \pi R^2$. Column 8 in Table 1 shows that the volumetric flow rate achievable by such an NCAM–EANE is approximately five times greater than that available in the EOF-driven microchannel ($Q = 165$ vs. 33 pL s^{-1}). Both structures can achieve a similarly high conversion efficiency, but due to this improvement in throughput, the total flow of the product species F_A is also much greater (column 9, Table 1), up to $F_A = 16.5$ versus 3.14 pmol s^{-1}. Overall, a far superior performance is achievable by the NCAM–EANE, in a much smaller space, than by the microband–microchannel system.

3.6. Effect of Electrokinetic Transport and Structure Dimensions

Taking advantage of the calculations relating ψ to W, Pe, and η^* permits a set of conditions for optimal operation of nanochannel electrodes to be identified. **Figure 6** shows that the optimal steady-state current for a mass-transport-limited electron-transfer reaction at an EANE can be obtained over a range of electrode dimensions, $W > 0.5$, and Peclet number, $Pe > 0.3$ at $\eta^* = 1$. It is important to place these results into context numerically. Using the values for r and D cited above, the optimal Peclet number is reached at linear velocities of the order 1 mm s^{-1}, a very commonly encountered velocity for electrokinetic transport in NCAMs[34] and certainly reached under the conditions used to acquire the cyclic voltammetry data in Figure 3. Since the Peclet number is a function of μ_{eo}, which is determined by the polymer surface chemistry and the pH, Figure 6 is also broadly applicable to a variety of reactor materials and accompanying conditions. Furthermore, the data in Figure 3 were acquired with an EANE geometry

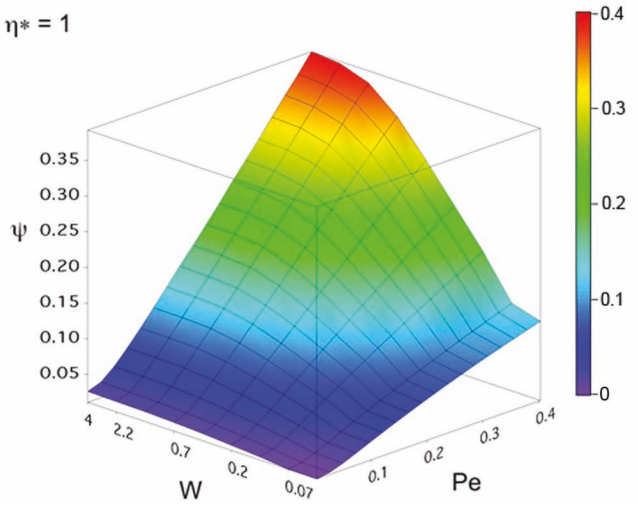

Figure 6. Plot of dimensionless current ψ as a function of Peclet number and electrode width for high kinetic overpotential, $\eta^* = 1$. As such, the exact value of the equilibrium potential E_0 is unimportant, so long as a transport-limited condition can be achieved. The predictive value of ψ derived from this plot is therefore applicable to a wide variety of electrochemical reactions, based on the design parameters W and Pe for a particular EANE–nanocapillary geometry and electroosmotic mobility.

that translates to $W \approx 0.6$, a value that is also well within the optimal range shown in Figure 6.

4. Conclusion

Both experiments and simulations confirm that NCAM–EANE structures serve as highly efficient nanoscale reactors capable of electrochemical conversion and subsequent transport of products downstream for additional processing. Further, the electrochemical conversion efficiency of these devices compares favorably to that of larger microchannels when the comparison is made on the basis of dimensionless parameters. Additionally, controlled molecular transport of reacted species away from the reaction site in the nanochannel takes a fraction of the time that it would take in a microchannel. Simulation results confirm that the reactor dimensions play a crucial role in determining conversion efficiency, and an aspect ratio that achieves optimum performance with minimal electrode material is identified. The faradaic current depends on both Peclet number and reactor dimensions in the region where electron transfer becomes highly responsive to the kinetic overpotential due to mass-transport limitations. Under these conditions, optimal performance for the NCAM–EANE electrochemical reactors described here can be achieved in ranges of parameter space corresponding to common materials, applied potentials, flow rates, and electrode dimensions. Under particularly favorable conditions, namely $Pe > 0.3$, $W > 0.5$, it is possible to achieve conversion efficiencies of 100%. Thus, these simulations describe the design considerations broadly applicable to accomplishing high-efficiency electrochemical conversions in the NCAM–EANE structure.

NANO MICRO small

5. Experimental Section

Device Construction: The device containing the array of EANEs was fabricated by a previously described method.[29] Briefly, 2 nm Cr and 200 nm Au were vacuum evaporated onto a clean glass slide to form the QRE. Then an SU-8 layer (7 μm thick) was applied by spin-coating, exposure, and development according to the manufacturer's specifications. A second layer of metal, 2 nm Cr/200 nm Au/2 nm Cr, was deposited again by thermal deposition atop the first layer of SU-8 forming the EANE. A second SU-8 layer was then applied as described above. Contact to the QRE was established by wet-chemical etching of a microwell through the opposite side of the glass coverslip. One or more arrays of nanopores, 11 × 11 pores, were patterned sequentially by focused ion beam milling, each nanopore presenting a diameter in the range 500–700 nm. The experimental results presented herein are for a single array, 121 pores for which the diameters are 600 ± 60 nm. Finally, two polydimethylsiloxane (PDMS) microwells were added to the device constituting reservoirs of electroactive species on either side of the EANE-containing NCAM.

Cyclic Voltammetry: Devices were vacuum filled with a series of solutions containing ferricyanide (10 mM < $[Fe(CN)_6^{3-}]$ < 100 mM) in 1 M KNO_3/10 mM phosphate, pH 7.2. Linear cyclic voltammetry was performed at a 50 mV s^{-1} scan rate, supplied by a potentiostat (Gamry Reference 600, Gamry Instruments, Warminster, PA) controlled by the Gamry Framework software package. A background scan was first performed on the phosphate buffer in the absence of ferricyanide, and the faradaic current was obtained by subtracting this background current from that measured during ferri/ferrocyanide cyclic voltammetry.

Simulations: Finite element simulations were carried out using COMSOL Multiphysics v. 4.2a (Bandon, MA). Time-dependent studies incorporating three physical models were used: 1) creeping flow, 2) electrostatics, and 3) transport of dilute species. Physical and geometric parameters were set to: R = 250 nm, h = 15 μm, 10 nm ≤ w ≤ 1 μm, $D_A = 6.5 \times 10^{-10}$ m^2 s^{-1}, and $\mu_{eo} = 4.5 \times 10^{-8}$ m^2 V^{-1} s^{-1}.[35] Model-specific boundary conditions are described in the Supporting Information.

Supporting Information

Supporting Information is available from the Wiley Online Library or from the author.

Acknowledgements

This work was supported by the National Science Foundation grant NSF0852741, the Department of Energy Basic Energy Sciences DE FG02 07ER15851, and by the Army Corp of Engineers contract W9132-10-0010.

[1] J. I. Yeh, H. B. Shi, *WIREs Nanomed. Nanobiotechnol.* **2010**, *2*, 176
[2] M. Dimaki, P. Vazquez, M. H. Olsen, L. Sasso, R. Rodriguez-Trujillo, I. Vedarethinam, W. E. Svendsen, *Sensors* **2010**, *10*, 10339.
[3] M. H. Yang, F. L. Qu, Y. S. Lu, Y. He, G. L. Shen, R. Q. Yu, *Biomaterials* **2006**, *27*, 5944.
[4] Y. H. Yang, G. M. Yang, Y. Huang, H. P. Bai, X. X. Lu, *ColloidsSurf. A* **2009**, *340*, 50.
[5] S. J. Kim, S. H. Ko, K. H. Kang, J. Han, *Nat.Nanotechnol.* **2010**, *5*, 297.
[6] A. Piruska, S. Branagan, D. M. Cropek, J. V. Sweedler, P. W. Bohn, *Lab Chip* **2008**, *8*, 1625.
[7] A. Piruska, S. P. Branagan, A. B. Minnis, Z. Wang, D. M. Cropek, J. V. Sweedler, P. W. Bohn, *Lab Chip* **2010**, *10*, 1237.
[8] R. W. Murray, *Chem.Rev.* **2008**, *108*, 2688.
[9] D. M. Nelumi, T. Perera, T. Ito, *Analyst* **2010**, *135*, 172.
[10] V. Garcia-Morales, K. Krischer, *J.Chem.Phys.* **2011**, *134*, 244512.
[11] P. Sun, M. V. Mirkin, *Anal.Chem.* **2006**, *78*, 6526.
[12] M. Rimboud, R. D. Hart, T. Becker, D. W. M. Arrigan, *Analyst* **2011**, *136*, 4674.
[13] P. Sun, *Anal.Chem.* **2010**, *82*, 276.
[14] B. Zhang, Y. H. Zhang, H. S. White, *Anal.Chem.* **2004**, *76*, 6229.
[15] B. Zhang, Y. H. Zhang, H. S. White, *Anal.Chem.* **2006**, *78*, 477.
[16] S. G. Lemay, E. D. Goluch, B. Wolfrum, P. S. Singh, M. A. G. Zevenbergen, *Anal.Bioanal.Chem.* **2009**, *394*, 447.
[17] B. Wolfrum, E. Katelhon, B. Hofmann, S. G. Lemay, M. A. G. Zevenbergen, A. Offenhausser, *Anal.Chem.* **2010**, *82*, 8502.
[18] D. W. M. Arrigan, *Analyst* **2004**, *129*, 1157.
[19] H. S. White, A. Bund, *Langmuir* **2008**, *24*, 12062.
[20] H. S. White, B. Zhang, Y. H. Zhang, *Anal.Chem.* **2004**, *76*, 6229.
[21] W. B. Zimmerman, *Chem.Eng.Sci.* **2011**, *66*, 1412.
[22] N. V. Rees, *Russ.J.Electrochem.* **2006**, *44*, 368.
[23] N. A. Lacher, K. E. Garrison, R. S. Martin, S. M. Lunte, *Electrophoresis* **2001**, *22*, 2526.
[24] C. Amatore, N. Da Mota, C. Lemmer, C. Pebay, C. Sella, L. Thouin, *Anal.Chem.* **2008**, *80*, 9483.
[25] C. Amatore, N. Da Mota, C. Sella, L. Thouin, *Anal.Chem.* **2007**, *79*, 8502.
[26] C. Amatore, N. Da Mota, C. Sella, L. Thouin, *Anal.Chem.* **2010**, *82*, 2434.
[27] N. M. Contento, S. P. Branagan, P. W. Bohn, *Lab Chip* **2011**, *11*, 3634.
[28] E. C. Anderson, M. C. Weston, I. Fritsch, *Anal.Chem.* **2010**, *82*, 2643.
[29] S. P. Branagan, N. M. Contento, P. W. Bohn, *J.Am.Chem.Soc.* **2012**, *134*, 8617.
[30] H. C. Chang, L. Y. Yeo *Electrokinetically DrivenMicrofluidics and Nanofluidics*, Cambridge University Press, Cambridge **2010**.
[31] T. M. Squires, M. Z. Bazant, *J. Fluid Mech.* **2004**, *509*, 217.
[32] P. Dutta, A. Beskok, *Anal.Chem.* **2001**, *73*, 1979.
[33] E. N. Gatimu, T. L. King, J. V. Sweedler, P. W. Bohn, *Biomicrofluidics* **2007**, *1*, 021502.
[34] T. C. Kuo, D. M. Cannon, Y. N. Chen, J. J. Tulock, M. A. Shannon, J. V. Sweedler, P. W. Bohn, *Anal.Chem.* **2003**, *75*, 1861.
[35] T. Sikanen, S. Tuomikoski, R. A. Ketola, R. Kostiainen, S. Franssila, T. Kotiaho, *Lab Chip* **2005**, *5*, 888.

Received: January 31, 2012
Revised: June 15, 2012
Published online: August 21, 2012

